



# Neurolastin, a dynamin family GTPase, translocates to mitochondria upon neuronal stress and alters mitochondrial morphology *in vivo*

Received for publication, December 19, 2018, and in revised form, June 3, 2019. Published, Papers in Press, June 7, 2019. DOI 10.1074/jbc.RA118.007245

Richa Madan Lomash<sup>†1</sup>, Ronald S. Petralia<sup>§</sup>, Lynne A. Holtzclaw<sup>¶</sup>, Mumeko C. Tsuda<sup>||</sup>, Ya-Xian Wang<sup>§</sup>, John D. Badger II<sup>‡</sup>, Heather A. Cameron<sup>||</sup>, Richard J. Youle<sup>\*\*</sup>, and Katherine W. Roche<sup>‡2</sup>

From the <sup>†</sup>Receptor Biology Section and <sup>\*\*</sup>Surgical Neurology Branch, NINDS, National Institutes of Health, Bethesda, Maryland 20892, the <sup>§</sup>Advanced Imaging Core, NIDCD, National Institutes of Health, Bethesda, Maryland 20892, the <sup>¶</sup>Microscopy and Imaging Core, NICHD, National Institutes of Health, Bethesda, Maryland 20892, and the <sup>||</sup>Section on Neuroplasticity, NIMH, National Institutes of Health, Bethesda, Maryland 20892

Edited by Phyllis I. Hanson

Neurolastin is a dynamin family GTPase that also contains a RING domain and exhibits both GTPase and E3 ligase activities. It is specifically expressed in the brain and is important for synaptic transmission, as neurolastin knockout animals have fewer dendritic spines and exhibit a reduction in functional synapses. Our initial study of neurolastin revealed that it is membrane-associated and partially co-localizes with endosomes. Using various biochemical and cell-culture approaches, we now show that neurolastin also localizes to mitochondria in HeLa cells, cultured neurons, and brain tissue. We found that the mitochondrial localization of neurolastin depends upon an N-terminal mitochondrial targeting sequence and that neurolastin is imported into the mitochondrial intermembrane space. Although neurolastin was only partially mitochondrially localized at steady state, it displayed increased translocation to mitochondria in response to neuronal stress and mitochondrial fragmentation. Interestingly, inactivation or deletion of neurolastin's RING domain also increased its mitochondrial localization. Using EM, we observed that neurolastin knockout animals have smaller but more numerous mitochondria in cerebellar Purkinje neurons, indicating that neurolastin regulates mitochondrial morphology. We conclude that the brain-specific dynamin GTPase neurolastin exhibits stress-responsive localization to mitochondria and is required for proper mitochondrial morphology.

Dynamin family GTPases are key membrane-remodeling mechanoenzymes. They are localized to specific organelles and govern proper organellar morphology (1). For example, atlastin, an ER<sup>3</sup>-

localized dynamin GTPase, drives ER membrane fusion (2). Drp1, OPA1, and mitofusins are examples of mitochondrial GTPases that mediate fission and fusion to maintain the dynamic mitochondrial network (3).

We recently identified and characterized neurolastin (RNF112/Znf179) as a new member of the dynamin family of GTPases. Neurolastin is a developmentally regulated brain-specific protein (4, 5) that is important for proper synaptic transmission. Neurolastin knockout (KO) animals have smaller brains, fewer dendritic spines, less functional synapses, reduced paired pulse facilitation, altered neurotransmitter receptor levels, and smaller endosomes (6). In another study, Tsou *et al.* (7) also reported reduced brain size and impaired brain functions (motor balance, spatial learning, and memory) in neurolastin KO mice. At the molecular level, neurolastin displays a unique combination of GTPase and RING domains. It can hydrolyze GTP to GMP and exhibits E3 ligase activity. Neurolastin is peripherally associated with membranes via a hydrophobic region and has a partial cytosolic and endosomal localization (6).

E3 ubiquitin ligases are enzymes of the ubiquitin proteasome system that conjugate ubiquitin to substrate proteins and regulate signaling or turnover via proteasomal degradation (8). Examples in the literature illustrating the influence of ubiquitination on the dynamin GTPases include regulation of the mitochondrial fission GTPase Drp1 by the E3 ligase MARCH5 and of the yeast mitofusin Fzo1 by Mdm30-mediated ubiquitination (9, 10). This ubiquitin-mediated regulation of dynamin GTPases serves as a quality control mechanism for maintaining mitochondrial dynamics. Both dynamin GTPases and E3 ligases are essential for proper functioning of the subcellular machinery and also play diverse roles in brain function. Dynamin has known roles in synaptic vesicle endocytosis, neurotransmission, and memory formation (11–13). Atlastin regulates axon elongation and dendritic spine morphogenesis (14, 15). Mitofusin-2 dysfunction has a strong association with mul-

This work is supported by intramural funding of the NINDS, National Institutes of Health (NIH); NIDCD (NIH)–Advanced Imaging Core; NICHD (NIH)–Microscopy and Imaging Core; and NIMH (NIH). The authors declare that they have no conflicts of interest with the contents of this article. The content is solely the responsibility of the authors and does not necessarily represent the official views of the National Institutes of Health.

This article contains Figs. S1–S6.

<sup>1</sup> To whom correspondence may be addressed: Receptor Biology Section, NINDS, Porter Neuroscience Research Center, Bldg. 35, Rm. 2C-903, Bethesda, MD 20892. E-mail: richa.madanlomash@nih.gov.

<sup>2</sup> To whom correspondence may be addressed: Receptor Biology Section, NINDS, Porter Neuroscience Research Center, Bldg. 35, Rm. 2C-903, Bethesda, MD 20892. E-mail: roche@ninds.nih.gov.

<sup>3</sup> The abbreviations used are: ER, endoplasmic reticulum; KO, knockout; KI, knockin; HA, hemagglutinin; PNS, post-nuclear supernatant; CC, coiled-coil; Hp, hydrophobic patch; O/A, oligomycin and antimycin A; CytC, cyto-

chrome c; STED, stimulated emission depletion microscopy; DIV, day(s) *in vitro*; FOV, field(s) of view; OMM, outer mitochondrial membrane; IMM, inner mitochondrial membrane; aa, amino acid(s); RT, room temperature; PFA, paraformaldehyde; NGS, normal goat serum; BrdU, bromodeoxyuridine; mtDNA, mitochondrial DNA; COX, cytochrome c oxidase; GAPDH, glyceraldehyde-3-phosphate dehydrogenase; IMS, intermembrane space.

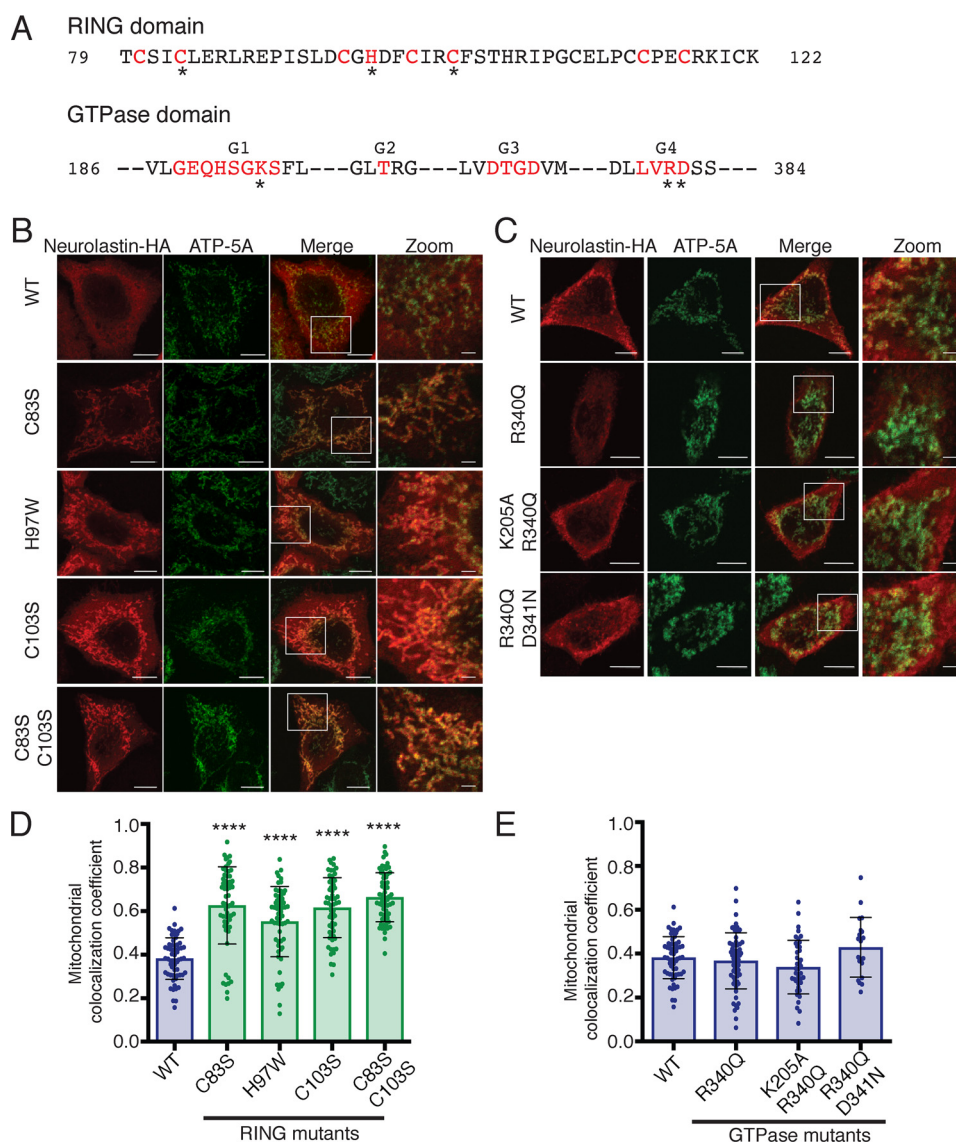


**Figure 1. RING mutants of neurolastin localize to mitochondria.** A, critical residues in the RING (residues 79–122) and GTPase domain (residues 186–384) of neurolastin are highlighted in red. Mutated residues are labeled with an asterisk. B and C, neurolastin-HA (WT, RING, or GTPase mutants) was expressed in HeLa cells and visualized by immunostaining with  $\alpha$ -HA (red). Mitochondria were labeled with  $\alpha$ -ATP5A (green). Merged and enlarged images in the two right panels show colocalization. Graphs in D and E depict the Mander's colocalization coefficient between endogenous ATP5A and neurolastin-HA ( $n = 3$ ,  $n = 20$ /experiment; blinded experiment). Statistics were done by comparing different mutants with WT neurolastin using Dunnett's multiple-comparison test. \*\*\*\*,  $p = 0.0001$ ; scale bars, 10 and 2  $\mu\text{m}$  (enlarged image). See also Fig. S1. Error bars, S.D.

tiple neurological diseases (16). Additionally, ubiquitination pathways regulate turnover of different synaptic receptors and scaffolding proteins (17, 18). Defects in these proteins are linked to various disease conditions, including different neurological disorders (19–21). Interestingly, of all of the known dynamins, even though some are enriched in the brain, neurolastin is the only known brain-specific family member.

In this study, we demonstrate a novel and unexplored role of neurolastin in regulating mitochondrial structure. We show that neurolastin is imported into the mitochondrial intermembrane space (IMS) via its N terminus. Although at steady state neurolastin exhibits partial cytosolic, endosomal, and mitochondrial localization, it has increased translocation to the mitochondria upon induction of cellular stress and mitochondrial fragmentation in neuronal cells. The RING domain of neurolastin and the mitoprotease Lon1 regulate the localization and

expression of neurolastin, respectively. Importantly, the neurolastin KO animals have fragmented mitochondria, indicating that neurolastin regulates mitochondrial morphology in the brain.

## Results

### RING mutants of neurolastin localize to mitochondria

At steady state, neurolastin showed both a partially diffuse distribution and a partial punctate localization representing its cytosolic and membrane-associated organellar forms, respectively. However, a catalytically inactive RING mutant of neurolastin (H97W) displayed a distinct mitochondrial localization in HeLa cells while being excluded from other organelles (6). Although surprising, this was a robust phenotype, and thus we explored it in more detail. First, we mutated other critical residues of the RING domain (H97W, C83S, C103S, and C83S/C103S; Fig. 1A) and

## Neuroplastin alters mitochondrial morphology

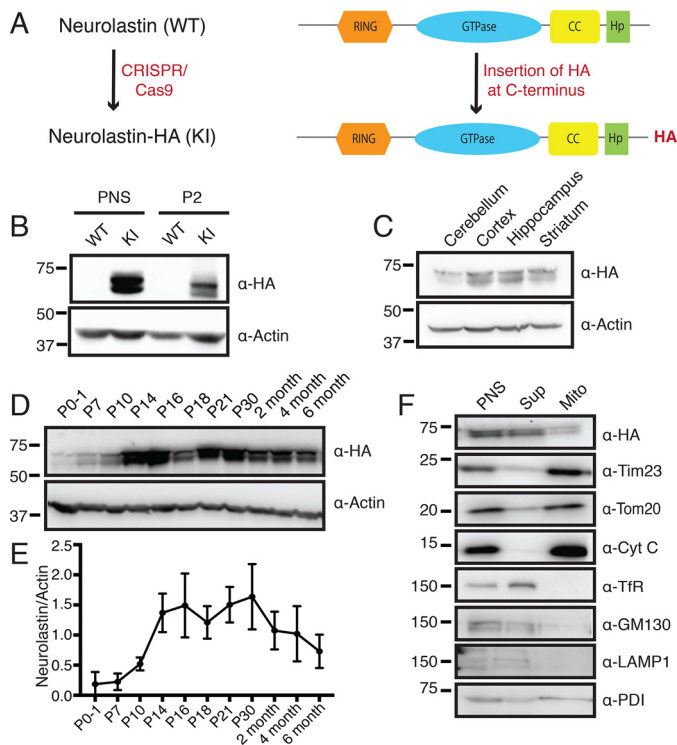


**Figure 2. Neuroplastin is developmentally regulated and present on mitochondria.** *A*, schematic of neuroplastin-HA-tagged KI mouse. *B*, Western blotting shows specific detection of endogenous neuroplastin from KI mouse with the HA antibody. *P2*, synaptosomal fraction. WT mice were used as controls. *C*, PNS from 3-week-old KI mice shows the presence of neuroplastin in different brain regions. *D*, developmental regulation of neuroplastin protein expression was observed by Western blotting of PNS from KI brains. *P*, days post-natal. The graph in *E* shows average expression level from three different animals of the indicated ages. *F*, mitochondria were isolated from 6-week-old KI mice. Mitochondrial enrichment is confirmed by the presence of different mitochondrial proteins Tom20 (OMM marker), Tim23 (IMM marker), and CytC (IMS marker) in the enriched mitochondrial preparation. *Sup*, supernatant; *Mito*, mitochondria. Immunoblotting with α-HA confirms the presence of endogenous neuroplastin in the mitochondria from KI brain. See also Fig. S2. Error bars, S.D.

tested the mitochondrial localization of these mutants by measuring Mander's colocalization coefficient between neuroplastin mutants and the mitochondrial marker, ATP5A (Fig. 1, *B* and *D*). The stability and expression of the mutants was tested biochemically, revealing similar levels of expression (Fig. S1, *A* and *B*). We found that a mutation in the RING domain leads to increased mitochondrial localization of neuroplastin. Subsequently, we also mutated critical residues of the GTPase domain (R340Q, K205A/R340Q, and R340Q/D341N; Fig. 1*A*) and tested the mitochondrial localization of these mutants. The GTPase mutants showed a diffuse distribution and punctate localization similar to WT neuroplastin (Fig. 1, *C* and *E*). These results confirm that inactivation of the RING domain leads to increased mitochondrial localization of neuroplastin.

### Endogenous neuroplastin is developmentally regulated and present on mitochondria

To examine the mitochondrial presence of neuroplastin *in vivo*, we generated knockin (KI) mice with an HA tag appended to the C terminus of neuroplastin (Fig. 2*A*). The tag was added at the C terminus and not the N terminus based on the observation that neuroplastin with an N-terminal tag has very weak expression (data not shown). The KI animals were generated to

visualize endogenous neuroplastin due to lack of a specific antibody. The precise insertion of HA at the correct location was confirmed by genotyping, sequencing, and Western blotting of the post-nuclear supernatant (PNS) and synaptosomal (*P2*) fraction (Fig. S2 and Fig. 2*B*). We subsequently characterized the protein's expression in the KI and were able to determine that endogenous neuroplastin is expressed in different brain regions upon Western blotting (Fig. 2*C*). We observed multiple species of neuroplastin on a Western blot (around the expected molecular mass of ~72 kDa). This was similar to our previous observations where more than one protein species around the expected molecular weight in the neuroplastin KO animals was absent (6). Although we do not know the identity of the two protein bands, they may represent the different isoforms of neuroplastin. Subsequently, we tested the developmental profile of neuroplastin using PNS isolated from the brain of different aged animals. As reported previously (5), we also observed that neuroplastin's expression is developmentally regulated. Interestingly, we noticed that neuroplastin levels peak between 2 and 4 weeks of age, after which the expression decreased (Fig. 2, *D* and *E*).

To identify the cell populations that express neuroplastin, we performed immunohistochemistry from brains of KI animals but encountered technical limitations with the HA antibody. Thus, we performed immunohistochemistry on sagittal brain sections of neuroplastin KO mice generated previously (6). The neuroplastin gene has been replaced with a LacZ reporter in the KO. Neuroplastin expression patterns were visualized by fluorescence detection of a β-gal antibody. We observed neuroplastin expression in neurons and some astrocyte populations, whereas no signal was detected in microglia (Fig. S3).

We finally prepared an enriched mitochondria fraction from the brains of the KI animals (Fig. 2*F*). We tested mitochondrial enrichment by blotting for classical mitochondrial markers, Tim23, Tom20, and cytochrome *c* (CytC). In the same preparation, we detected endogenous neuroplastin-HA, confirming its presence in brain mitochondria. Other organellar markers—transferrin receptor (TfR, an endocytic marker), GM130 (Golgi), and LAMP1 (lysosomal protein)—were not detected, although a slight ER contamination (protein-disulfide isomerase, PDI) was seen in the enriched mitochondrial fraction.

### The N terminus of neuroplastin is required for mitochondrial localization

Neuroplastin is a multidomain protein containing a RING, GTPase, and predicted coiled-coil (CC) domain. We previously demonstrated that it has a hydrophobic patch (Hp), which mediates membrane association (6). In addition to these defined domains, neuroplastin has ~70 aa at the N terminus and ~100 aa at the C terminus that do not conform to any known motifs. To determine what region mediates mitochondrial targeting of neuroplastin, we generated different deletion constructs. For visualization by immunofluorescence microscopy, a C-terminal HA tag was added to all of the constructs. The expression of different truncations was tested biochemically (Fig. S1*C*). While all of the constructs migrated at the expected molecular weight, variation in their expression level was observed, possibly due to varying stability of the truncations.

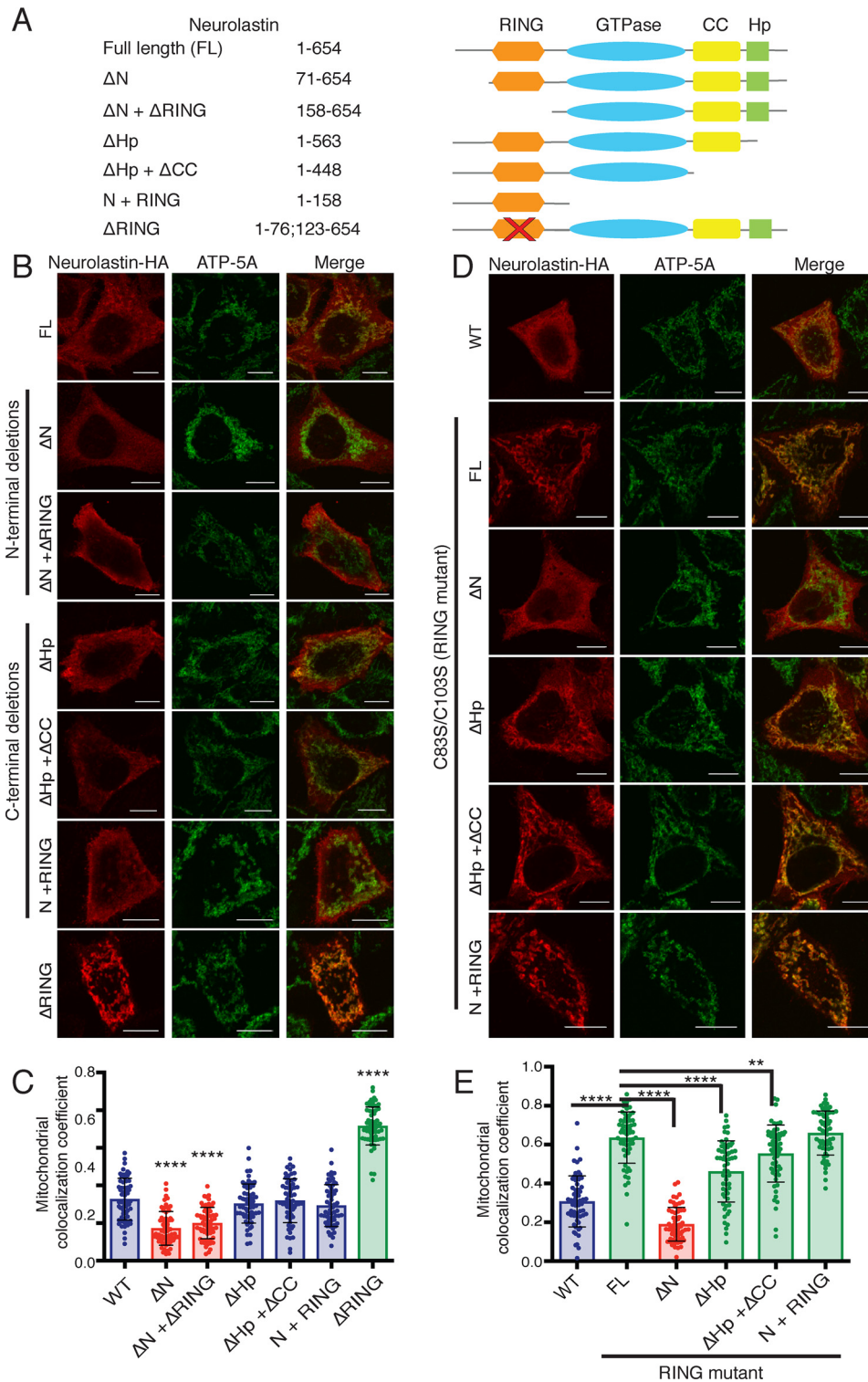


**Figure 3. The N terminus of neurolastin is important for mitochondrial targeting.** *A*, pictorial representation of different domains and truncations of neurolastin (RING (orange), GTPase (blue), coiled-coil (yellow), hydrophobic (green)). Neurolastin-HA (FL and different truncations) were generated on a WT (*B*) or RING mutant backbone (*D*), expressed in HeLa cells, and visualized by immunostaining with  $\alpha$ -HA (red) and  $\alpha$ -ATP5A (green). Merged images in the right panel show colocalization. Graphs in *C* and *E* indicate the Mander's colocalization coefficient between endogenous ATP5A and neurolastin-HA ( $n = 3$ ,  $n = 20$ /experiment; blinded experiment). Statistics were done by comparing different mutants with WT neurolastin in *C* and WT or C83S/C103S (FL) neurolastin in *E* as indicated. Statistics were done by comparing different mutants with WT neurolastin in *C* and C83S/C103S (FL) in *E* using Dunnett's multiple-comparison test: \*\*\*\*,  $p = 0.0001$ ; \*\*,  $p = 0.003$ . Scale Bar, 10  $\mu$ m. See also Fig. S1. Error bars, S.D.

We measured mitochondrial localization of different neurolastin truncations defined in the schematic (Fig. 3A): full-length (FL) (residues 1–654); N-terminal deletions  $\Delta N$  (residues

71–654) and  $\Delta N + \Delta RING$  (residues 158–654); and C-terminal deletions  $\Delta Hp$  (residues 1–563),  $\Delta Hp + \Delta CC$  (residues 1–448), N + RING (residues 1–158), and  $\Delta RING$  chimera (residues

## Neurolastin alters mitochondrial morphology

1–76 and 123–654). The data in Fig. 3 (B and C) are a measure of colocalization between C-terminal HA-tagged neurolastin and ATP5A. Compared with FL neurolastin, the C-terminal deletions ( $\Delta$ Hp,  $\Delta$ Hp+ $\Delta$ CC, and N+RING) showed a similar level of colocalization, although the N-terminal deletions ( $\Delta$ N and  $\Delta$ N+ $\Delta$ RING) had a significantly reduced mitochondrial localization. We observed a robust increase in mitochondrial localization of the  $\Delta$ RING chimera in which only the RING domain is deleted, leaving the N terminus and the rest of the protein intact. The distinct mitochondrial localization of the  $\Delta$ RING chimera, as well as the RING mutants, show that an active RING domain inhibits mitochondrial localization of neurolastin, although it does not completely exclude neurolastin from the mitochondria, as the WT protein shows significantly more mitochondrial localization compared with  $\Delta$ N neurolastin. Reduced mitochondrial colocalization with both N-terminal deletion constructs suggests that the N terminus is important for mitochondrial targeting. Based on these observations, we tested whether the N terminus is vital by analyzing the localization of the neurolastin RING mutant. We truncated the N terminus in one of our tested RING mutants to generate C83S/C103S ( $\Delta$ N). We also generated C-terminal deletions on the C83S/C103S background, tested expression of all of these constructs (Fig. S1D), and analyzed their localization (Fig. 3, D and E). As expected, neurolastin C83S/C103S (FL) showed significantly increased mitochondrial localization compared with WT protein, whereas neurolastin C83S/C103S ( $\Delta$ N) failed to target to the mitochondria, confirming that the N terminus of neurolastin is essential for mitochondrial targeting. We also tested neurolastin C83S/C103S C-terminal deletion constructs and found that the localization phenotype is similar to that of neurolastin C83S/C103S (FL). A slight reduction in mitochondrial localization observed for neurolastin C83S/C103S ( $\Delta$ Hp and  $\Delta$ Hp+ $\Delta$ CC) may be due to altered protein conformation in the deletion constructs.

### Neurolastin is imported into the mitochondrial IMS

The transport of newly synthesized proteins into the mitochondria often depends on a mitochondrial targeting sequence (MTS), generally located at the N termini of proteins (22, 23). When a protein is imported into the mitochondria, the MTS from the precursor protein is usually cleaved, resulting in a mature processed form. Upon analyzing the protein sequence of neurolastin, multiple bioinformatic tools predicted an N-terminal MTS in neurolastin with a high degree of confidence by comparing shared physicochemical properties between MTS of known proteins (Fig. 4A). These predictions prompted us to test whether neurolastin is imported into the mitochondria. We expressed neurolastin in HeLa cells and added oligomycin and antimycin A (O/A) to dissipate the mitochondrial membrane potential and block import and processing of precursor proteins. Under normal conditions, we observed two bands on an immunoblot of WT and RING mutant neurolastin, presumably the FL neurolastin protein and a smaller processed mitochondria-localized form (Fig. 4B). After O/A treatment, the processed form of neurolastin disappeared in cells expressing either neurolastin WT or the RING mutant. Neurolastin  $\Delta$ N lacking the MTS was used as a control that migrated as a single

molecular weight species and remained unaltered upon O/A treatment (Fig. 4B). The ratio of mitochondrially imported (processed) to cytosolic (preprotein) full-length protein was plotted and found to be significantly reduced for the mitochondrially targeted WT neurolastin and RING mutant upon O/A treatment, whereas  $\Delta$ N levels were not changed (Fig. 4C). We also analyzed the localization of WT, RING mutant, and  $\Delta$ N neurolastin upon O/A treatment by imaging individual cells and found a striking difference in the distribution of the RING mutant protein that changed from being mitochondrial to a completely diffuse distribution due to mitochondrial membrane potential disruption upon O/A treatment, confirming mitochondrial import (Fig. 4D). We noted a slight discrepancy between results from imaging and biochemical analysis of mitochondrial import possibly due to differences in the techniques employed. Using immunofluorescence microscopy, the neurolastin RING mutant showed much higher mitochondrial localization compared with WT protein, whereas the biochemical data did not show a significant difference, although the observed trend was similar to the immunofluorescence observations.

We immunoprecipitated neurolastin overexpressed in HeLa cells and, using mass spectrometry analysis, identified Lon1 as a putative interacting partner of the RING mutant (data not shown). Lon1 is a highly conserved ATP-dependent mitoprotease that is imported into the mitochondrial matrix and is crucial for mitochondrial homeostasis (24). To determine whether neurolastin is regulated by Lon1, we inhibited the protease activity by using the synthetic triterpenoid CDDO. We saw a significant increase in the expression of neurolastin WT and RING mutant protein, whereas no change was observed for the neurolastin  $\Delta$ N mutant (Fig. 4, E and F).

To test whether the N terminus of neurolastin is sufficient to target any cytosolic protein to the mitochondria, we tested localization of GFP fused to different lengths of the neurolastin MTS. We found that whereas GFP alone or 23-GFP had a diffuse distribution, both 38-GFP and 78-GFP showed mitochondrial localization (Fig. 4, G and H), confirming that the N terminus of neurolastin is a *bona fide* MTS.

As neurolastin is imported into the mitochondria, we wanted to discern whether it is imported into the IMS or is present in the matrix. To determine the submitochondrial localization of neurolastin, we expressed the GFP-tagged RING mutant of neurolastin (C83S/C103S) and immunostained under different permeabilization conditions. GFP expression was seen in all conditions, and neurolastin (GFP) staining (in red) was observed both by digitonin and Triton X-100 permeabilization. This was similar to staining for CytC, an IMS marker, whereas the matrix protein, Hsp70, could be stained only using Triton X-100 permeabilization. No signal was detected in control cells without any permeabilization (Fig. 5, A and B). Subsequently, using stimulated emission depletion microscopy (STED), we showed that neurolastin colocalizes with the IMS proteins (CytC and OPA1) (Fig. 5, C and D). These observations confirm that neurolastin is imported into the mitochondrial IMS.

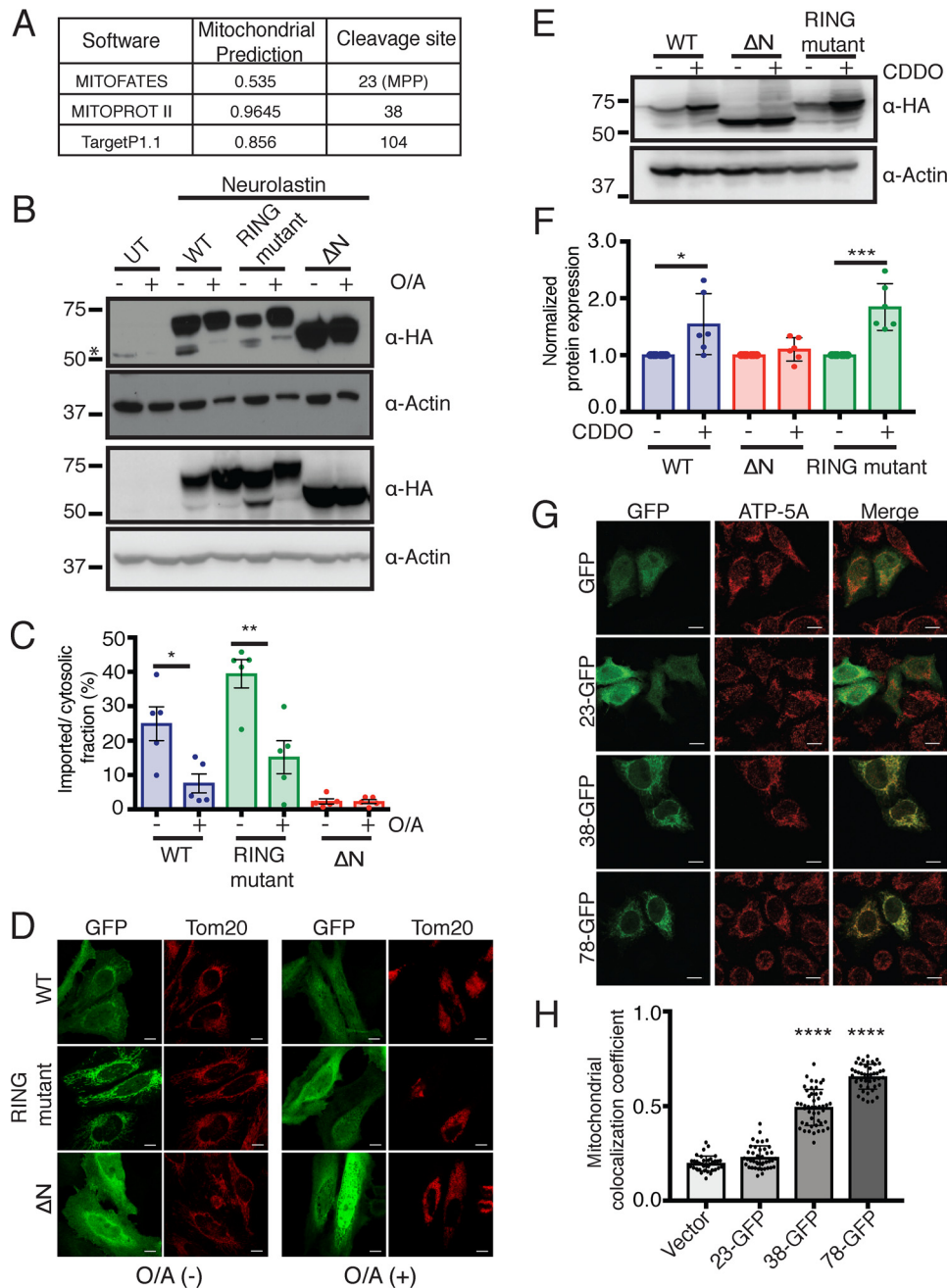


**Figure 4. Neurolastin is imported into the mitochondria.** *A*, mitochondrial localization prediction scores for neurolastin using different bioinformatic tools. Localization probability ranges from 0 (least probable) to 1 (highly probable). These tools also predict the possible site of MTS cleavage. *MPP*, mitochondrial processing peptidase. *B–F*, different mutants of neurolastin were transfected into HeLa cells and treated with *O/A* (24 h) to dissipate mitochondrial membrane potential or CDDO (6 h) to inhibit Lon1 protease activity. Neurolastin  $\Delta N$  (lacking the MTS) was used as a control. *B*, disappearance of the smaller-sized protein shows no preprotein processing for WT and RING mutant of neurolastin in the presence of *O/A*. Two representative examples are shown. A faint nonspecific band (\*) slightly lower than the processed form is observed in certain experiments. The *graph* in *C* shows quantification of the imported protein and is presented as a ratio of imported (processed)/cytosolic (preprotein) fraction of neurolastin ( $n = 5$ , *t* test; \*\*,  $p = 0.005$ ; \*,  $p = 0.015$ ;  $p = 0.059$  when comparing WT (–*O/A*) with RING mutant (–*O/A*), suggesting a trend similar to results observed in imaging experiments). *D*, confocal micrographs showing change in protein localization upon *O/A* treatment in individual cells; Tom20 labeling shows disruption of mitochondrial structure upon *O/A* treatment. *E*, increase in expression of WT and RING mutant upon CDDO treatment suggests Lon1-mediated regulation of neurolastin’s expression. The *graph* on the right (*F*) is quantification of protein expression normalized to respective actin levels ( $n = 6$ , *t* test; \*\*\*,  $p = 0.0005$ ; \*,  $p = 0.03$ ). *G*, neurolastin MTS (different lengths) was fused to the N terminus of GFP, and the mitochondrial localization ( $\alpha$ -ATP5A) of these GFP fusion constructs is analyzed. The *graph* in *H* indicates the Mander’s colocalization coefficient between endogenous ATP5A and MTS-GFP ( $n = 4$ ,  $n = 10–15$  cells/experiment). Statistics were done by comparing different constructs with GFP control using Dunnett’s multiple-comparison test: \*\*\*\*,  $p = 0.0001$ . Scale bar, 10  $\mu$ m. Error bars, S.D.

**The neurolastin RING domain and N terminus regulate mitochondrial localization in neurons**

Because neurolastin is primarily a brain-specific protein, we sought to validate our findings in cultured primary neurons. To

confirm that neurolastin mutants show a similar localization to mitochondria in neurons, we co-expressed neurolastin-HA mutants and mito-GFP (to label mitochondria) in day *in vitro* (DIV) 10 hippocampal neurons and stained them at DIV 13

## Neurolastin alters mitochondrial morphology

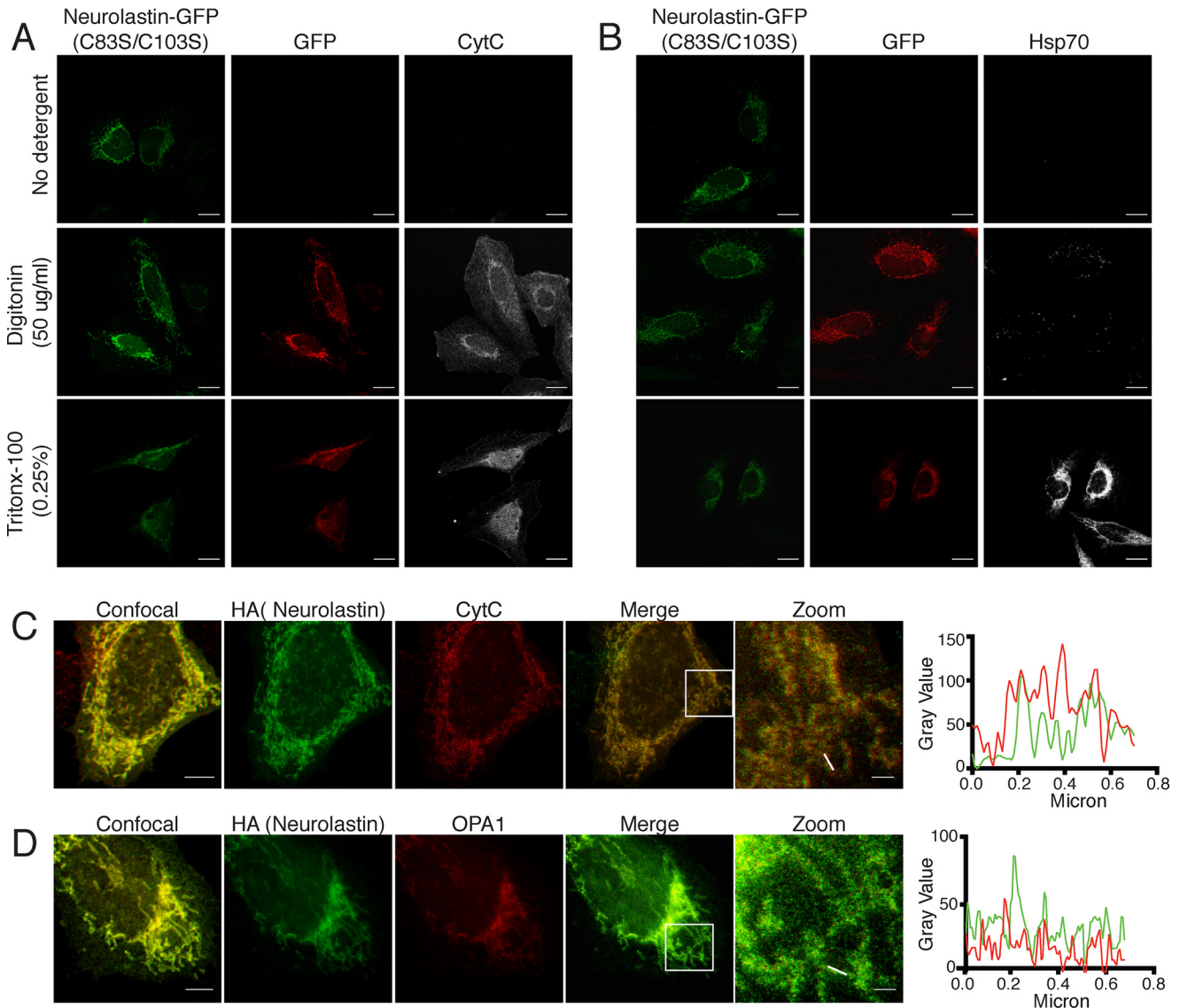


**Figure 5. Neurolastin is imported into the mitochondrial IMS.** Neurolastin-GFP (C83S/C103S) was expressed in HeLa cells, which were permeabilized using different detergents (digitonin, 50  $\mu$ g/ml) or (Triton X-100, 0.25%) and stained for GFP and CytC (IMS marker) or Hsp70 (matrix marker). Panels show GFP fluorescence (green),  $\alpha$ -GFP (red), and  $\alpha$ -CytC (white) (A) or  $\alpha$ -Hsp70 (white) (B). A no detergent condition was used as a negative control. Scale bar, 20  $\mu$ m. C and D, dual-color STED imaging of neurolastin-HA (C83S/C103S) in HeLa cells with endogenous IMS markers: CytC (C) and OPA1 (D). Left, confocal micrograph followed by STED images (individual channels, merge, and enlarged region). Scale bar, 5  $\mu$ m. Plots on the right show the intensity profiles across the indicated mitochondria (line drawn in the enlarged image; scale bar, 1  $\mu$ m).

(Fig. 6A). Mitochondrial localization was measured by scoring colocalization in dendrites between the two markers (Fig. 6B). Similar to observations in HeLa cells, neurolastin WT and the GTPase mutant (R340Q/D341N) had comparable mitochondrial localization, whereas neurolastin RING mutant (C83S/C103S) and  $\Delta$ N displayed a significant increase or decrease in mitochondrial localization, respectively. These data confirm that the RING domain and N terminus govern neurolastin's mitochondrial localization in neurons as well.

### Neurolastin translocates to mitochondria in response to cellular stress and mitochondrial fragmentation

Imaging both in HeLa cells and neurons showed that neurolastin at steady state is partially localized to the mitochondria, whereas the inactivation of the RING domain leads to increased mitochondrial localization. We wanted to determine the phys-

iological stimuli, such as synaptic activity, intracellular trafficking regulation, or mitochondrial disruption, that would produce a similar effect. To test this, we cultured hippocampal neurons from KI animals until DIV 16 to allow detectable expression of neurolastin and subsequently treated them with different compounds: (a) KCl, tetrodotoxin, bicuculine, and glutamate (used for regulation of synaptic activity); (b) inhibitors (leupeptin (lysosomes), okadaic acid (phosphatases), and MG132 (proteasomes)); and (c) antimycin A for depolarization of mitochondrial membranes. To determine the mitochondrial localization, we double-labeled with HA and Tom20 to detect endogenous neurolastin and mitochondria, respectively, and measured colocalization by quantifying Pearson's coefficient from the dendrites of neurons. We observed a significant increase in mitochondrial localization of neurolastin upon glutamate treatment

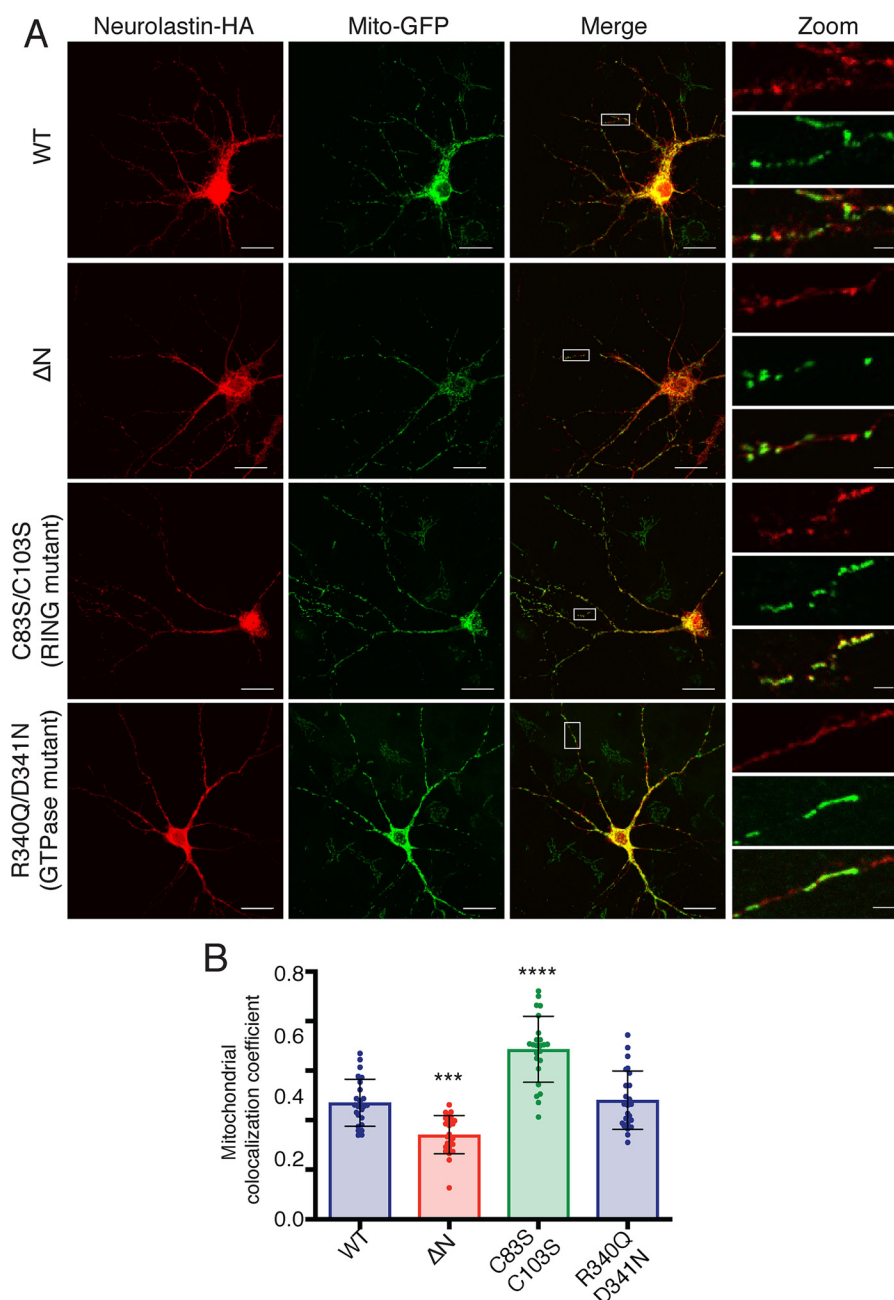


**Figure 6. The RING domain regulates mitochondrial localization of neurolastin in neurons.** *A*, hippocampal neurons were co-transfected with mito-GFP and neurolastin-HA at DIV 10, stained at DIV 13 with  $\alpha$ -HA (red) and  $\alpha$ -GFP (green), and imaged. Scale bars, 10 and 1  $\mu$ m (enlarged image). *B*, Mander's colocalization co-efficient was quantified to determine mitochondrial localization of different neurolastin constructs. Three dendritic regions were analyzed per neuron ( $n = 3$ ,  $n = 8$ /experiment; blinded experiment). Statistics of different constructs were done by comparing with WT neurolastin (using Dunnett's multiple-comparison test; \*\*\*,  $p = 0.0002$ ; \*\*\*\*,  $p = 0.0001$ ). Error bars, S.D.

(Fig. 7, *A* and *B*), which causes induction of cellular stress leading to mitochondrial fragmentation.

#### Neurolastin KO has smaller but more numerous mitochondria

We have previously demonstrated that neurolastin is a functional dynamin GTPase (6) and now show that neurolastin is localized to the mitochondria. To examine the functional importance of neurolastin *in vivo*, we compared the mitochondrial structure between WT and neurolastin KO mice. We evaluated the mitochondria in sections from different brain regions. Whereas we observed mitochondrial alterations in

both the hippocampus and cerebellum, we also noticed differences in the number of neurons in the hippocampus when comparing WT *versus* KO animals. Upon further investigation, we found this to be a result of defective adult neurogenesis in neurolastin KO animals (Fig. S4).

To avoid this confounding factor, we analyzed the mitochondrial structure from cerebellar Purkinje neurons. We found that the neurolastin KO mice contain smaller mitochondria compared with WT (Fig. 8, *A* and *B*). Quantification of mitochondria from multiple fields of view (FOV) showed that the mitochondrial area and the maximum and minimum Feret's

## Neurolastin alters mitochondrial morphology

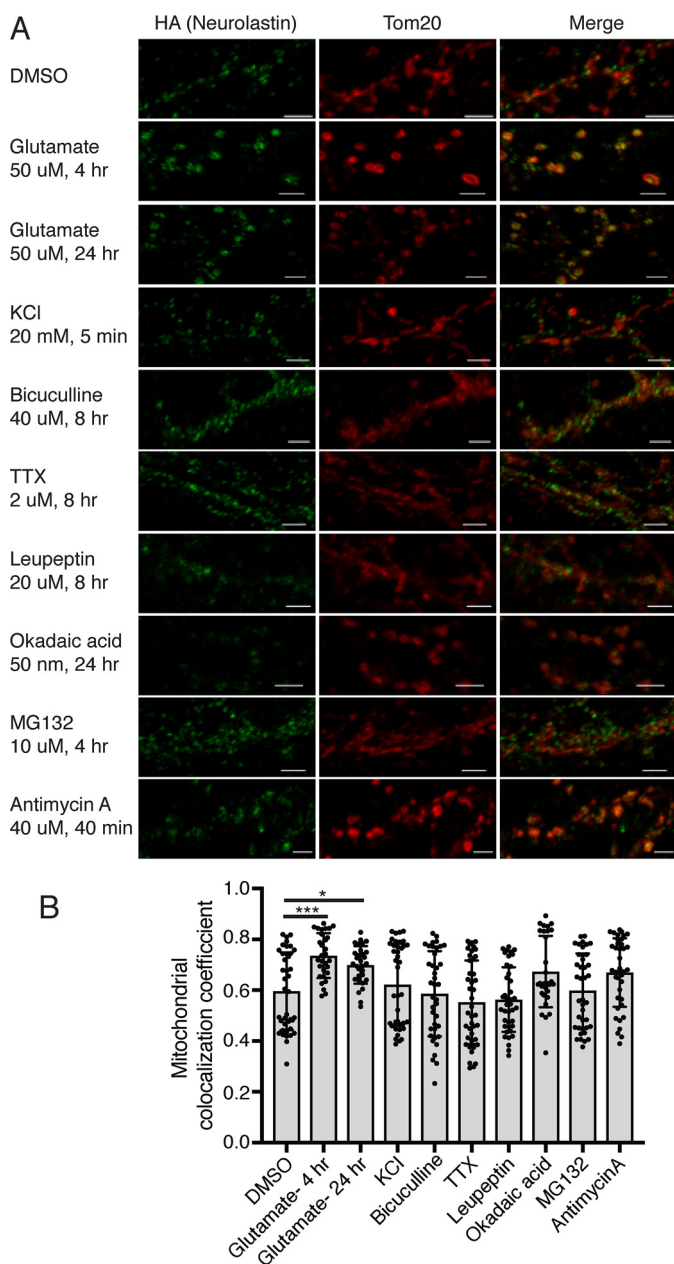


**Figure 7. Endogenous neurolastin translocates to mitochondria upon cellular stress and mitochondrial fragmentation.** A, DIV 16 hippocampal neurons isolated from KI mice were treated with the indicated drugs, and localization of endogenous neurolastin with mitochondria was determined by staining with  $\alpha$ -HA and  $\alpha$ -Tom20. B, graph shows colocalization between HA and Tom20. Three dendritic regions per neuron were quantified and compared with DMSO-treated cells ( $n = 3$ ,  $n = 10$ /experiment; blinded experiment; Dunnett's multiple-comparison test; \*\*\*,  $p = 0.0005$ ; \*,  $p = 0.0194$ ). Scale bar, 10  $\mu$ m. Error bars, S.D.

diameter were reduced in the KO (Fig. 8, C, E, and G). The panels on the right (Fig. 8, D, F, and H) show the change in frequency of mitochondrial size, revealing a shift toward smaller size in the KO. We also counted the mitochondrial number and found that the neurolastin KO mice have a significantly greater number of mitochondria, also depicted in the frequency distribution per FOV (Fig. 8, I and J). We calculated the total mitochondrial area per cell and found no significant change (WT,  $1.069 \pm 0.044223 \mu\text{m}^2$ ; KO,  $0.9803 \pm 0.03324 \mu\text{m}^2$ ). Consistent with this, the mtDNA copy number (Fig. S5)

in WT and neurolastin KO was similar. Cristae structure is another important aspect of mitochondrial dynamics, and we observed no discernable change in the cristae structure between WT and KO (Fig. S6). Taken together, these results show that neurolastin alters only the mitochondrial morphology and neither the cristae structure nor the total mitochondrial mass.

## Discussion

Neurolastin is the newest addition to the dynamin family of GTPases (6, 25). It has characteristics common to other dynamin family members: GTP hydrolysis, self-association, and membrane localization. Additionally, neurolastin possesses a RING domain and exhibits E3 ligase activity, making it unique among other dynamin family proteins (6).

Neurolastin is essential for proper brain function, as neurolastin KO animals have severe defects in motor skills, spatial learning and memory, brain size, synaptic transmission, dendritic spine density, and endosome volume (6, 7). In the current study, we show that neurolastin KO animals also have altered mitochondrial structure, specifically smaller but a larger number of mitochondria as observed in the KO brain. Mitochondria are highly dynamic organelles that are subject to trafficking and quality control and continually undergo cycles of fission and fusion enabled by multiple mitochondrial proteins. It is well-established that mitochondrial trafficking is important in neurons and several molecules involved have been identified along with their underlying pathways (26, 27). For maintenance of fission–fusion balance, the known dynamin family GTPases, Drp1 (a fission GTPase) and Mfn1/Mfn2 and OPA1 (fusion GTPases) are critical (3). We also found involvement of neurolastin in regulating adult neurogenesis. This is consistent with strong evidence in the literature showing how neurogenesis is regulated by mitochondrial morphology and dynamics, either via metabolic balance alterations or by guiding the fate of neuronal stem cells (28); future experiments will uncover the exact mechanism by which neurolastin regulates adult neurogenesis.

In the brain, mitochondria perform numerous cellular functions, including ATP production,  $\text{Ca}^{2+}$  signaling, ROS homeostasis, and neurotransmitter metabolism, to support the energy demands of specialized brain functions. Mitochondrial function is also vital in controlling fundamental processes of synaptic plasticity, including neurite outgrowth, neurogenesis, neurotransmitter release, and dendritic remodeling. Disturbances in mitochondrial dynamics are linked to impaired synaptic plasticity and multiple neurodegenerative disorders (29–31). As examples, smaller mitochondria as a result of increased Drp1 levels (more fission) are associated with ALS, Huntington's disease, and Alzheimer's disease, whereas reduced levels of Mfn2 and OPA1 (less fusion) are responsible for Charcot-Marie Tooth disease A2 and autosomal dominant optic atrophy, respectively (29). In addition to the defective synaptic transmission in neurolastin KO animals that we have observed (6), RNA-Seq and microarray data from ALS and Alzheimer's disease mouse models reveal changes in expression of neurolastin, thus implicating its role in maintaining neuronal health (32, 33). The neuroprotective role is strengthened by our current observation that neurolastin exhibits increased transloca-

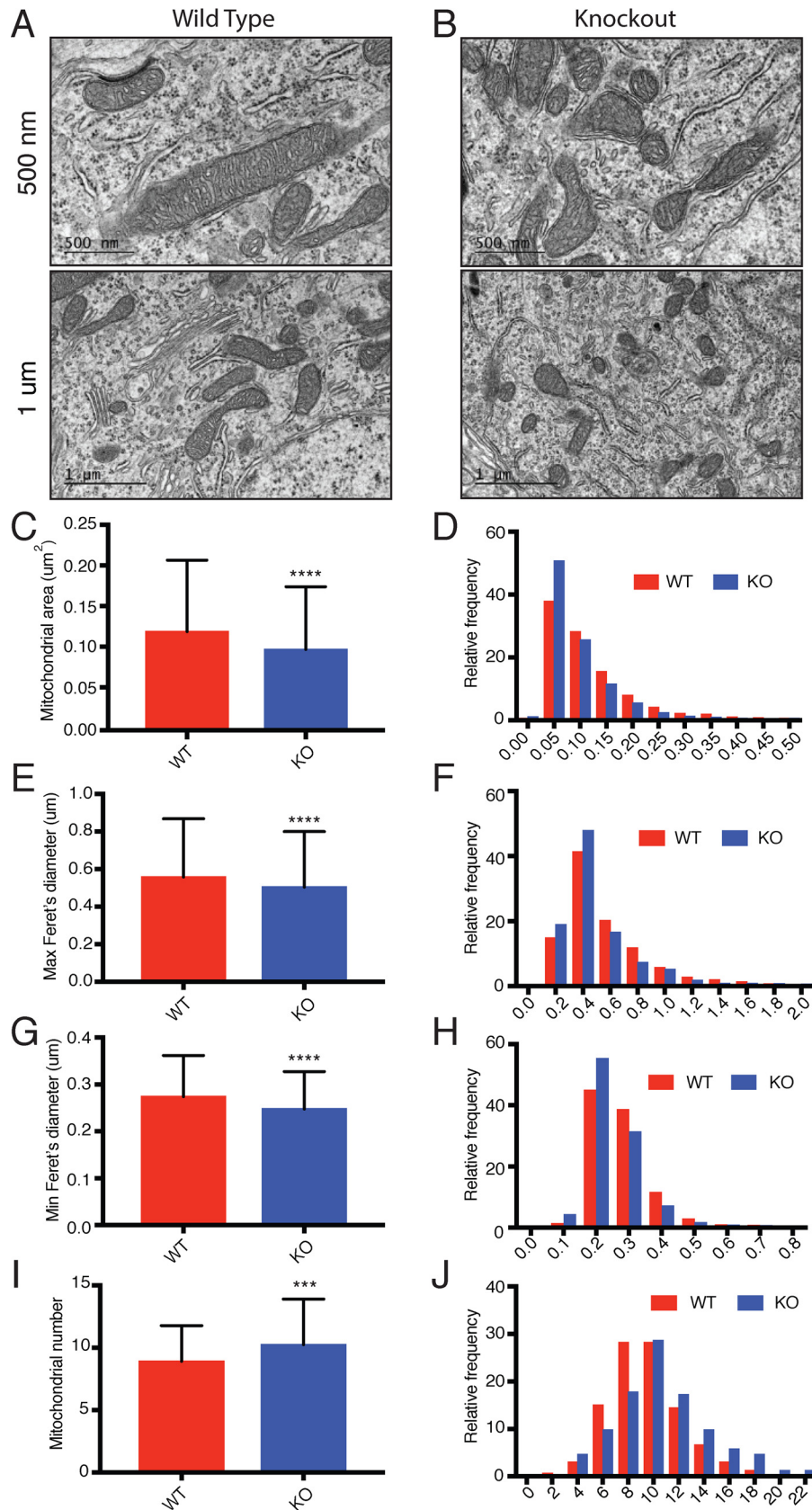


**Figure 8. Neurolastin KO mice have smaller-sized mitochondria.** A and B, representative electron micrographs from the soma of cerebellar Purkinje neurons of 4-month-old WT and KO animals. The number of mitochondria analyzed was as follows: WT ( $n = 1505$ ) and KO ( $n = 1804$ ) from two animals each. Graphs show quantification and distribution (relative frequency) of the area of each mitochondrion (C and D), maximum Feret's diameter (E and F), minimum Feret's diameter (G and H), and number of mitochondria per FOV (I and J). Statistics were done by comparing WT and KO using an unpaired *t* test (\*\*\*\*,  $p < 0.0001$ ; \*\*\*,  $p = 0.0002$ ). See also Figs. S5 and S6. Error bars, S.D.

## Neurolastin alters mitochondrial morphology

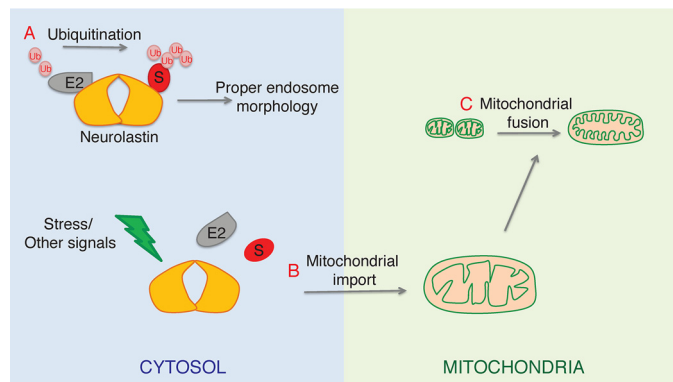


**Figure 9. Proposed mechanism of neurolastin function.** A, in the cytosol, neurolastin partners with an E2 conjugating enzyme to potentially target substrates (S), which facilitates partial endosomal localization and normal endosomal morphology. B, neurolastin is imported into the mitochondria via the N-terminal MTS. The import is expedited upon detecting cellular stress and possibly other signals. C, neurolastin drives mitochondrial fusion to maintain a healthy mitochondrial network.

tion to the mitochondria upon induction of cellular stress. This result is supported by recent findings that implicate neurolastin in protecting neuronal cells against oxidative stress following injury (34–36) and in regulating the neuropathy protein, TDP-43 (37).

We have demonstrated that neurolastin in steady state is present at multiple subcellular locations—endosomes, mitochondria, and cytosol—where it performs distinct functions. Cytosolic/endosomal neurolastin governs proper endosomal morphology, for which it requires intact E3 ligase activity, presumably to target substrates (Fig. 9A). This is supported by observations that the RING mutant of neurolastin does not localize to and cannot rescue the endosomal size defect in KO neurons (6). Neurolastin is imported into the mitochondria via an N-terminal MTS (Fig. 9B). This conclusion is drawn from characterization of the neurolastin MTS, followed by validation of mitochondrial import and localization using imaging and biochemical assays. Once imported into the mitochondria, neurolastin may govern mitochondrial fusion (Fig. 9C), as we observed more fragmented mitochondria in the neurolastin KO animals without a change in total mitochondrial mass. At any given time, it is possibly the mitochondria-localized fraction of neurolastin that drives the mitochondrial fusion utilizing energy by GTP hydrolysis. Because there is no reported ubiquitin inside the mitochondria, the E3 ligase activity is likely to be limited to the non-mitochondrial neurolastin. As observed, a functional RING domain blocks mitochondrial targeting of neurolastin, possibly via concealing the MTS. Cellular stress or other signals may introduce post-translational modifications or disrupt any protein interactions to facilitate a conformational change exposing the MTS and expedite mitochondrial import of neurolastin, an aspect to be explored in future structural studies.

Neurolastin can now be added to the existing list of dynamins that localize to and alter mitochondrial dynamics (3). Neurolastin has unique characteristics and also shares similarities when compared with these mitochondrial GTPases. Drp1 is mostly cytosolic but cycles to the outer mitochondrial membrane (OMM) via phosphorylation (38–40); additionally, Drp1

mediates peroxisomal fission (41). Similarly, neurolastin also localizes to and affects morphology of two organelles, mitochondria and endosomes. Mitofusins are present at the OMM and facilitates fusion, whereas OPA1 is imported into the mitochondrial IMS, where it mediates IMM fusion and maintains the cristae structure (42–44). Similar to OPA1, neurolastin is also imported into the mitochondrial IMS, and the fragmented mitochondria in the neurolastin KO mice confirm its role in mitochondrial fusion. Mitochondria have a very robust quality control system to balance the fission–fusion processes, and mediators of these processes are controlled via protein–protein interactions and post-translational modifications (29). Specifically, Drp1 function is affected by phosphorylation, nitrosylation, and sumoylation (45); mitofusins are also post-translationally regulated by ubiquitination, phosphorylation, and acetylation (29). OPA1 has the most complex regulation: post-transcriptionally, it undergoes alternative splicing, giving rise to eight splice variants followed by post-translational proteolytic cleavage by different mitochondrial proteases (46). In a similar fashion, we find that neurolastin’s expression is influenced by Lon1 protease. Lon1 was previously thought to be important only for degradation of misfolded proteins; however, there is emerging evidence that it plays an important regulatory role in mitochondrial homeostasis (24). Although Lon1 is a matrix protease, there is evidence that it interacts with subunits of the TIM (translocase of inner membrane) and MICOS (mitochondrial contact site and cristae-organizing system) complex, both found in the IMM. It has also been reported that depletion of Lon1 leads to a stress response (47). Our data suggest increased mitochondrial localization of neurolastin during cellular stress, and it will be interesting to discern whether Lon1 regulates neurolastin only under stress conditions. We also detail another regulatory mechanism of neurolastin’s localization being governed by its functional RING domain. There may also exist other mechanisms for controlling neurolastin expression and function, as we observed multiple isoforms of the protein and a developmental change in its expression. Drp1, OPA1, and Mfn1/2 are ubiquitously expressed with evidence of a Drp1 brain-specific isoform at the RNA level (48). Neurolastin is distinctive as it is brain-specific. In protein database searches, neurolastin orthologues could only be found in vertebrates that have a well-developed nervous system, consistent with its brain-specific localization and function. In conclusion, neurolastin is a brain-specific dynamin GTPase that regulates the membrane dynamics of endosomes and mitochondria, thus affecting neurotransmission.

## Experimental procedures

### Plasmid constructs

Full-length mouse neurolastin (residues 1–654) with a C-terminal HA tag was generated as described previously (6). Different truncations:  $\Delta N$  (residues 71–654),  $\Delta N + \Delta RING$  (residues 158–654),  $\Delta Hp$  (residues 1–563),  $\Delta Hp + \Delta CC$  (residues 1–448),  $N + RING$  (residues 1–158), and  $\Delta RING$  chimera (residues 1–76 and 123–654) were PCR-amplified using specific primers and cloned with a C-terminal HA tag into pcDNA3.1 in EcoRI/NotI sites. Point mutations were generated

using the QuikChange mutagenesis protocol (Agilent Technologies). Neurolastin-GFP constructs were cloned in pEGFP-N1 with GFP fused at the C terminus in EcoRI/BamHI sites. The plasmids were sequenced to confirm introduction of the required mutation. For overexpression in neurons, the plasmids were subcloned into pCAG vector. Mito-GFP has been described previously (49). MTS constructs were generated by fusing different lengths of the N-terminal of neurolastin (23, 38, and 78 aa) to GFP in pEGFP-N1 vector. The choice of lengths was made based on bioinformatic predictions. 78-GFP was cloned as it contains the entire N terminus before the start of the RING domain.

### Antibodies and reagents

**Immunofluorescence**—The following antibodies were used:  $\alpha$ -ATP5A (Abcam 15H4C4 (1:1000)),  $\alpha$ -HA (Abcam ab9110 (1:1000) or Roche Applied Science 11867431001 (1:500)),  $\alpha$ -Tom20 (Santa Cruz Biotechnology, Inc., sc-17764 (1:200) or Santa Cruz Biotechnology sc-11415 (1:200)),  $\alpha$ -GFP (Life Technologies, Inc., A10262 (1:500)),  $\alpha$ -cytochrome *c* (BD Biosciences 556433 (1:200)),  $\alpha$ -OPA1 (BD Biosciences 612606 (1:200)), and  $\alpha$ -Hsp70 (Thermo Fisher Scientific MA3-028 (1:1000)).

**Immunohistochemistry**—The following antibodies were used:  $\alpha$ - $\beta$ Gal (Abcam ab134435 (1:2500)),  $\alpha$ -Iba1 (Abcam ab5076 (1:500)),  $\alpha$ -NeuN (Millipore MAB377 (1:500)),  $\alpha$ -calbindin (Swant CB-38 (1:1000)), and  $\alpha$ -S100B (Sigma S2532 (1:1000)).

**Western blotting**— $\alpha$ -HA (Roche Applied Science 11867431001 (1:1000)),  $\alpha$ -actin (abm G043 (1:1000)),  $\alpha$ -tubulin (Sigma T8328 (1:5000)),  $\alpha$ -Tom20 (Santa Cruz Biotechnology sc-17764 (1:1000)),  $\alpha$ -Tim 23 (BD Biosciences 611222 (1:1000)),  $\alpha$ -cytochrome *c* (BD Biosciences 556433 (1:1000)),  $\alpha$ -TfR (Invitrogen 136800 (1:500)),  $\alpha$ -GM130 (BD Biosciences 610822 (1:250)),  $\alpha$ -LAMP1 (BD Biosciences 611042 (1:500)),  $\alpha$ -protein-disulfide isomerase (BD Biosciences 610947 (1:1000)).

Alexa Fluor secondary antibodies and Prolong Gold/Diamond antifade were from Life Technologies, Inc. High purity drugs, inhibitors, and chemicals were purchased from Sigma, Calbiochem, Millipore, or Tocris. The concentration and duration of drug treatments were determined based on previous literature.

### Animals used in the study

The use and care of animals in this study followed the guidelines of the National Institutes of Health Animal Research Advisory Committee. Neurolastin KO animals have been described previously (6). HA-tagged KI animals were generated by CRISPR/Cas9. HA tag was inserted at the C terminus using the mutagenic oligomer GTCCCTGATGTCCGCACCCTTCCTACTGCCTTTCACGTAATTTACAGCTTCGACATCTTGCTGCTAAGCGTAATCTGGAACATCGTATGGGTATTCTCTTTGGGTAGGGGCTCTCGGTCCCCTCCTTGAAC-TCTCT. The insertion of HA in between the last amino acid and the STOP codon was confirmed by PCR and sequencing. Founders (F1) were interbred with C57/BL6 WT mice to generate future generations, F2 and F3. F3 mice were used for breeding homozygous animals and future experiments. Note that during this process, a silent mutation got incorporated at aa 652 (LLQEE, CAG to CAA).

### Neuronal cultures

For overexpression experiments, primary hippocampal neurons were cultured from embryonic day 18 rat embryos as described previously (50). Mouse hippocampal neurons were isolated from P0-P1 pups of KI animals using a method described previously (6). The neurons were plated on poly-L-lysine-coated plates.

### Imaging and analysis

**Immunofluorescence**—HeLa cells were transfected with 500 ng of neurolastin-HA using the CalPhos mammalian transfection kit (Clontech) following the manufacturer's instructions. Staining was performed using standard procedures at RT. 20–24 h after transfection, the cells were fixed with 4% paraformaldehyde (PFA) for 10 min and permeabilized with 0.25% Triton X-100 for 10–15 min. Subsequently, the cells were blocked in 10% normal goat serum (NGS) for 30 min, followed by incubation with primary antibody diluted in 3% NGS for 45 min. The unbound antibody was washed with PBS, and cells were incubated with the secondary antibody diluted at 1:1000 in 3% NGS. The cells were mounted in Prolong Gold antifade reagent.

For O/A treatment, cells were treated with oligomycin (10  $\mu$ g/ml) and antimycin A (4  $\mu$ g/ml) 2 h before transfection to dissipate mitochondrial membrane potential. 18 h post-transfection, the cells were fixed and stained as described above. For determining submitochondrial localization, neurolastin-GFP (C83S/C103S) was transfected in HeLa cells as described. Cells were fixed and stained as described above. Permeabilization was performed differently, either using digitonin (50  $\mu$ g/ml) or Triton X-100 (0.25%) for 10 min at RT. No permeabilization control was done where no background staining was observed.

Rat hippocampal neurons at DIV 10 were co-transfected with mito-GFP (1  $\mu$ g) and neurolastin-HA (500 ng) cloned in pCAG vector using Lipofectamine 2000. The cells were fixed at DIV 13 in 4% PFA + 4% sucrose for 7 min, permeabilized with 0.25% Triton X-100 for 5 min, and stained with  $\alpha$ -HA and  $\alpha$ -GFP, followed by appropriate secondary antibodies for 1 h each at RT. For drug treatment, KI neurons were treated with respective drugs/inhibitors for the indicated times at DIV 15–16, fixed as above, and stained with  $\alpha$ -HA and  $\alpha$ -Tom20. Z-stacks were captured using a  $\times$ 63 oil immersion objective of an LSM 510 Meta Zeiss confocal microscope.

**Determining colocalization with mitochondria**—To determine how much neurolastin is localized to the mitochondria, the colocalization coefficients were calculated using the ImageJ plugin JaCoP. Mander's coefficient was calculated for all experiments except for drug treatment in KI neurons, where Pearson's coefficient was calculated due to considerable difference in intensity of red and green channels. A total of 50–60 cells/condition across three independent experiments were evaluated in HeLa cells. For neurons, three regions of interest in the dendrites were selected for each neuron ( $\sim$ 25–30 neurons from three independent experiments). Throughout the imaging experiments, only cells that expressed medium levels of the protein were analyzed; cells with very weak or high expression were not considered.

## Neurolastin alters mitochondrial morphology

**Immunohistochemistry**—Mice (WT and neurolastin KO, 6–8 weeks of age) were anesthetized with isoflurane and perfused (gravity feed) via the left ventricle with PBS, pH 7.4, to clear blood, followed by 40 ml of 4% PFA in PBS to fix the tissue. Brains were post-fixed for 18 h in the same fixative prior to dissection. All tissues were cryoprotected in 30% sucrose 24–48 h at 4 °C and then sectioned on a Leica SM2010R Sliding Microtome (Leica Biosystems, Nussloch, Germany) into 30- $\mu$ m floating sections. Sections were processed through an immunohistochemical protocol as described previously (51). Briefly, sections were blocked and permeabilized for 1 h in carrier solution (0.5% Triton X-100, 1% goat serum, and 0.5% BSA, EMD Millipore in 1 $\times$  PBS, pH 7.4). Sections were incubated in primary antibodies diluted in carrier solution (0.3% Triton X-100) at 4 °C overnight, followed by extensive washing. Secondary antibodies, diluted in carrier solution, were applied for 1 h at RT. Floating sections were mounted onto gelatin-coated slides, air-dried, and preserved under #1.5 German coverglasses using Prolong Diamond mounting medium. Z-stacks were acquired on an inverted LSM 780 confocal microscope with a Plan-Apochromat  $\times$ 20, 0.8 numerical aperture lens and were rendered as maximum-intensity projections. Tiles scans were acquired on an inverted LSM 800 confocal microscope with a  $\times$ 10/0.3 Plan Neofluar objective. Image intensities were optimized in Fiji. Negative controls (no primary antibody; no primary or secondary antibody) were included in each experiment to determine the level of nonspecific secondary antibody binding and sample autofluorescence. In all cases presented, autofluorescence was minimal, and nonspecific signal above autofluorescence was absent.

**STED microscopy**—HeLa cells were plated on #1.5 coverglasses and transfected with 500 ng of Neurolastin-HA (C83S/C103S). The cells were immunostained with  $\alpha$ -HA and  $\alpha$ -CytC/ $\alpha$ -OPA1 followed by Alexa Fluor 488 and Alexa Fluor 594 antibodies as described above. The coverglasses were mounted using Prolong Diamond antifade reagent. The confocal and STED images of the samples were obtained using a  $\times$ 100 objective on a Leica TCS SP8 3X STED microscope (Leica Microsystems). Parameters used were as follows: for HA (Alexa Fluor 488), excitation, 488 nm, 4%; depletion laser, 592 nm, 70%; WLL intensity, 3%; for CytC/Opa1 (Alexa Fluor 594), excitation, 594 nm, 5%; depletion laser, 775 nm, 70%; WLL intensity, 3%. The pinhole was set to 0.7 Airy units, and the pixel size was 25  $\mu$ m. Images of 1024  $\times$  1024 were captured at a scan speed of 400 Hz, line average of 2, and frame accumulations of 4. For confocal imaging, WLL was decreased. The line intensity plots were generated using Fiji.

### Biochemistry from HeLa cells

**Expression of different proteins**—Cells were transfected with the indicated constructs using Lipofectamine 2000. 40 h post-transfection, the cells were lysed, and proteins were extracted in SDS sample buffer. The expression levels were analyzed by Western blotting. To test Lon-mediated degradation, CDDO (10  $\mu$ M) was added the day after transfection to the cells for 6 h. Tubulin or Actin were used as loading controls as indicated. For immunoprecipitation, neurolastin-HA was overexpressed in

HeLa cells and immunoprecipitated using HA-agarose beads (Sigma) as described previously (6).

**Import assay**—HeLa cells were transfected with the indicated plasmids using Lipofectamine 2000.  $\sim$ 24 h post-transfection, oligomycin (10  $\mu$ g/ml) and antimycin A (4  $\mu$ g/ml) were added to the cells to disrupt mitochondrial membrane potential and block import and preprotein processing. 24 h after drug treatment, cells were lysed in SDS sample buffer and boiled at 95 °C for 10 min. The proteins were resolved on 8% SDS-PAGE and subjected to Western blotting with the indicated antibodies.

### Biochemistry from brain tissue

**Developmental profile**—Brain tissue was homogenized in PBS containing protease and phosphatase inhibitors and centrifuged at 800  $\times$  g for 10 min to generate the PNS. The PNS was centrifuged at 9200  $\times$  g for 20 min to generate the P2 (crude synaptosomal) fraction. 200  $\mu$ g of protein was loaded and resolved on 8% SDS-PAGE, followed by Western blotting with the indicated antibodies.

**Mitochondria isolation**—Mitochondria were isolated from 6-week-old KI animal brains using an Abcam mitochondria isolation kit for tissue (ab110168). Brain tissue (0.4 g) was homogenized in isolation buffer (500  $\mu$ l  $\times$  2 tubes) in a Dounce homogenizer (20 strokes) on ice. 50  $\mu$ g of protein from each fraction was resolved on 12% SDS-PAGE and subjected to Western blotting with the indicated antibodies.

### Electron microscopy

Adult animals (WT and Neurolastin KO, 3.5 months old) were anesthetized and perfused with 0.1 M phosphate buffer, followed by fixation in 4% PFA plus 2% glutaraldehyde in the same buffer at RT overnight (52). The brains were washed with PBS and sectioned with a vibratome at 125  $\mu$ m. The sections were washed with 0.1 M cacodylate buffer, fixed in 1% osmium tetroxide, washed, and then dehydrated in different concentrations of ethanol and 1% uranyl acetate in 50% ethanol. The sections were transferred to propylene oxide, embedded in epon, and heated at 64 °C for 48 h. Thin sections were cut and examined in a JEOL JEM-2100 transmission electron microscope, and micrographs of mitochondria were taken from cerebellar Purkinje cell soma from a random sample of the neuropil in the molecular layer of the cerebellar cortex.

Different parameters of mitochondrial morphology were analyzed using ImageJ. A total of 160–180 images from two different WT and KO animals were analyzed. All mitochondria in an individual image (FOV) were identified, and their area and Feret's diameter (maximum and minimum) were determined. The total mitochondria area was calculated per cell by multiplying average area by the average number of mitochondria (WT,  $n = 11$ ; KO,  $n = 10$ ). The bar graphs and frequency distribution were plotted using GraphPad prism. The cristae structure was analyzed visually in higher-magnification images.

### Neurogenesis

Adult WT and KO mice were intraperitoneally injected once with bromodeoxyuridine (BrdU; 200 mg/kg). After 3 weeks, mice were anesthetized with isoflurane and transcardially perfused with 4% PFA in PBS. Brains were fixed overnight and then

transferred to 20% sucrose for at least 24 h. Brains were sectioned coronally on a freezing sliding microtome at 40  $\mu\text{m}$  throughout the entire hippocampus. A 1:8 series of sections were stained for incorporated BrdU, for the endogenous immature neuron marker doublecortin, or for the mature neuronal marker NeuN using immunofluorescence or for the endogenous cell proliferation marker proliferating cell nuclear antigen using cobalt-enhanced 3,3'-diaminobenzidine immunohistochemistry as described previously (53). Sections were mounted onto slides under PVA-DAPCO or Permount. Total cell numbers were stereologically estimated by counting cells in a known fraction of sections throughout the entire dentate gyrus using a  $\times 40$  objective. Images for BrdU, NeuN, and doublecortin were captured on a Zeiss LSM780 confocal microscope.

### Determining mtDNA copy number

Brain regions (hippocampus and cerebellum) were isolated from females of the indicated age and frozen at  $-80^\circ\text{C}$ . Tissue was homogenized in PBS containing protease and phosphatase inhibitors. Subsequently, genomic DNA was isolated from the tissue using a Qiagen DNeasy blood and tissue kit. Real-time PCR was set up in three technical replicates per animal using 10 ng of template DNA and SYBR Green quantitative PCR mix. COX I and GAPDH were amplified as indicators of mtDNA and nuclear DNA, respectively.  $C_T$  values were calculated and the data were plotted as  $2^{-\Delta C_T}$  (54). Primers used were as follows: COX I, AGGCTTCACCTAGATGACACA and GTAGCGTTCGTGGTATTCCCTGAA; GAPDH, GCAGTGGCAAAGTGGAGATT and GAATTTGCCGTGAGTGGAGT.

### Bioinformatics

Mouse neurolastin sequence (NP\_033574.2) was analyzed using different online tools for determination of mitochondrial import probability and MTS prediction: MitoFates (55), MITOPROT II (56), and TargetP1.1 (57).

### Statistics

An unpaired two-tailed  $t$  test, analysis of variance multiple comparisons, and post hoc analyses were done as indicated to determine the significance of the data. Graphs are represented as mean  $\pm$  S.D.

**Author contributions**—R. M. L. and K. W. R. conceptualization; R. M. L., R. S. P., L. A. H., and M. C. T. data curation and formal analysis; R. M. L. validation; R. M. L. investigation; R. M. L., L. A. H., M. C. T., Y.-X. W., and J. D. B. I. methodology; R. M. L. writing-original draft; R. M. L. and K. W. R. project administration; R. M. L., L. A. H., M. C. T., H. A. C., R. S. P., and K. W. R. writing-review and editing; H. A. C., R. S. P., and K. W. R. funding acquisition; R. J. Y. and K. W. R. supervision.

**Acknowledgments**—We thank Roche and Youle laboratory members for helpful discussions. We thank the NINDS and NICHD (National Institutes of Health) microscopy and imaging facilities. We thank Jingqi Lei, Carl Haugen, and Lijin Dong (NEI, National Institutes of Health) for generating the neurolastin-HA knockin mice.

### References

1. Praefcke, G. J., and McMahon, H. T. (2004) The dynamin superfamily: universal membrane tubulation and fission molecules? *Nat. Rev. Mol. Cell Biol.* **5**, 133–147 [CrossRef Medline](#)
2. Rismanchi, N., Soderblom, C., Stadler, J., Zhu, P. P., and Blackstone, C. (2008) Atlantin GTPases are required for Golgi apparatus and ER morphogenesis. *Hum. Mol. Genet.* **17**, 1591–1604 [CrossRef Medline](#)
3. Pernas, L., and Scorrano, L. (2016) Mito-morphosis: mitochondrial fusion, fission, and cristae remodeling as key mediators of cellular function. *Annu. Rev. Physiol.* **78**, 505–531 [CrossRef Medline](#)
4. Orimo, A., Inoue, S., Ikeda, K., Sato, M., Kato, A., Tominaga, N., Suzuki, M., Noda, T., Watanabe, M., and Muramatsu, M. (1998) Molecular cloning, localization, and developmental expression of mouse brain finger protein (Bfp)/ZNF179: distribution of bfp mRNA partially coincides with the affected areas of Smith-Magenis syndrome. *Genomics* **54**, 59–69 [CrossRef Medline](#)
5. Pao, P. C., Huang, N. K., Liu, Y. W., Yeh, S. H., Lin, S. T., Hsieh, C. P., Huang, A. M., Huang, H. S., Tseng, J. T., Chang, W. C., and Lee, Y. C. (2011) A novel RING finger protein, Znf179, modulates cell cycle exit and neuronal differentiation of P19 embryonal carcinoma cells. *Cell Death Differ.* **18**, 1791–1804 [CrossRef Medline](#)
6. Lomash, R. M., Gu, X., Youle, R. J., Lu, W., and Roche, K. W. (2015) Neurolastin, a dynamin family GTPase, regulates excitatory synapses and spine density. *Cell Rep.* **12**, 743–751 [CrossRef Medline](#)
7. Tsou, J. H., Yang, Y. C., Pao, P. C., Lin, H. C., Huang, N. K., Lin, S. T., Hsu, K. S., Yeh, C. M., Lee, K. H., Kuo, C. J., Yang, D. M., Lin, J. H., Chang, W. C., and Lee, Y. C. (2017) Important roles of Ring finger protein 112 in embryonic vascular development and brain functions. *Mol. Neurobiol.* **54**, 2286–2300 [CrossRef Medline](#)
8. Deshaies, R. J., and Joazeiro, C. A. (2009) RING domain E3 ubiquitin ligases. *Annu. Rev. Biochem.* **78**, 399–434 [CrossRef Medline](#)
9. Cohen, M. M., Amiot, E. A., Day, A. R., LeBoucher, G. P., Pryce, E. N., Glickman, M. H., McCaffery, J. M., Shaw, J. M., and Weissman, A. M. (2011) Sequential requirements for the GTPase domain of the mitofusin Fzo1 and the ubiquitin ligase SCFMdm30 in mitochondrial outer membrane fusion. *J. Cell Sci.* **124**, 1403–1410 [CrossRef Medline](#)
10. Karbowski, M., Neutzner, A., and Youle, R. J. (2007) The mitochondrial E3 ubiquitin ligase MARCH5 is required for Drp1 dependent mitochondrial division. *J. Cell Biol.* **178**, 71–84 [CrossRef Medline](#)
11. Jaskolski, F., Mayo-Martin, B., Jane, D., and Henley, J. M. (2009) Dynamin-dependent membrane drift recruits AMPA receptors to dendritic spines. *J. Biol. Chem.* **284**, 12491–12503 [CrossRef Medline](#)
12. Fà, M., Staniszewski, A., Saeed, F., Francis, Y. I., and Arancio, O. (2014) Dynamin 1 is required for memory formation. *PLoS One* **9**, e91954 [CrossRef Medline](#)
13. Raimondi, A., Ferguson, S. M., Lou, X., Armbruster, M., Paradise, S., Giovedi, S., Messa, M., Kono, N., Takasaki, J., Cappello, V., O'Toole, E., Ryan, T. A., and De Camilli, P. (2011) Overlapping role of dynamin isoforms in synaptic vesicle endocytosis. *Neuron* **70**, 1100–1114 [CrossRef Medline](#)
14. Gao, Y., Jiang, T., Qu, C., Tao, H., Cao, H., Zhao, Y., Wang, Y., Qu, J., and Chen, J. G. (2013) Atlantin-1 regulates dendritic morphogenesis in mouse cerebral cortex. *Neurosci. Res.* **77**, 137–142 [CrossRef Medline](#)
15. Zhu, P. P., Soderblom, C., Tao-Cheng, J. H., Stadler, J., and Blackstone, C. (2006) SPG3A protein atlantin-1 is enriched in growth cones and promotes axon elongation during neuronal development. *Hum. Mol. Genet.* **15**, 1343–1353 [CrossRef Medline](#)
16. Filadi, R., Pendin, D., and Pizzo, P. (2018) Mitofusin 2: from functions to disease. *Cell Death Dis.* **9**, 330 [CrossRef Medline](#)
17. Lin, A. W., and Man, H. Y. (2013) Ubiquitination of neurotransmitter receptors and postsynaptic scaffolding proteins. *Neural Plast.* **2013**, 432057 [CrossRef Medline](#)
18. Haglund, K., and Dikic, I. (2012) The role of ubiquitylation in receptor endocytosis and endosomal sorting. *J. Cell Sci.* **125**, 265–275 [CrossRef Medline](#)
19. George, A. J., Hoffiz, Y. C., Charles, A. J., Zhu, Y., and Mabb, A. M. (2018) A comprehensive atlas of E3 ubiquitin ligase mutations in neurological disorders. *Front. Genet.* **9**, 29 [CrossRef Medline](#)

## Neurolastin alters mitochondrial morphology

20. Heymann, J. A., and Hinshaw, J. E. (2009) Dynamins at a glance. *J. Cell Sci.* **122**, 3427–3431 [CrossRef Medline](#)
21. Devine, M. J., and Kittler, J. T. (2018) Mitochondria at the neuronal presynapse in health and disease. *Nat. Rev. Neurosci.* **19**, 63–80 [CrossRef Medline](#)
22. Chacinska, A., Koehler, C. M., Milenkovic, D., Lithgow, T., and Pfanner, N. (2009) Importing mitochondrial proteins: machineries and mechanisms. *Cell* **138**, 628–644 [CrossRef Medline](#)
23. Schmidt, O., Pfanner, N., and Meisinger, C. (2010) Mitochondrial protein import: from proteomics to functional mechanisms. *Nat. Rev. Mol. Cell Biol.* **11**, 655–667 [CrossRef Medline](#)
24. Pinti, M., Gibellini, L., Nasi, M., De Biasi, S., Bortolotti, C. A., Iannone, A., and Cossarizza, A. (2016) Emerging role of Lon protease as a master regulator of mitochondrial functions. *Biochim. Biophys. Acta* **1857**, 1300–1306 [CrossRef Medline](#)
25. Daumke, O., and Praefcke, G. J. (2016) Invited review: mechanisms of GTP hydrolysis and conformational transitions in the dynamin superfamily. *Biopolymers* **105**, 580–593 [CrossRef Medline](#)
26. Schwarz, T. L. (2013) Mitochondrial trafficking in neurons. *Cold Spring Harb. Perspect. Biol.* **5**, a011304 [Medline](#)
27. Sheng, Z. H. (2014) Mitochondrial trafficking and anchoring in neurons: new insight and implications. *J. Cell Biol.* **204**, 1087–1098 [CrossRef Medline](#)
28. Khacho, M., and Slack, R. S. (2018) Mitochondrial dynamics in the regulation of neurogenesis: from development to the adult brain. *Dev. Dyn.* **247**, 47–53 [CrossRef Medline](#)
29. Flippo, K. H., and Strack, S. (2017) Mitochondrial dynamics in neuronal injury, development and plasticity. *J. Cell Sci.* **130**, 671–681 [CrossRef Medline](#)
30. Liesa, M., Palacín, M., and Zorzano, A. (2009) Mitochondrial dynamics in mammalian health and disease. *Physiol. Rev.* **89**, 799–845 [CrossRef Medline](#)
31. Cheng, A., Hou, Y., and Mattson, M. P. (2010) Mitochondria and neuroplasticity. *ASN Neuro* **2**, e00045 [CrossRef Medline](#)
32. Ferraiuolo, L., Heath, P. R., Holden, H., Kasher, P., Kirby, J., and Shaw, P. J. (2007) Microarray analysis of the cellular pathways involved in the adaptation to and progression of motor neuron injury in the SOD1 G93A mouse model of familial ALS. *J. Neurosci.* **27**, 9201–9219 [CrossRef Medline](#)
33. Kim, K. H., Moon, M., Yu, S. B., Mook-Jung, I., and Kim, J. I. (2012) RNA-Seq analysis of frontal cortex and cerebellum from 5XFAD mice at early stage of disease pathology. *J. Alzheimers Dis.* **29**, 793–808 [CrossRef Medline](#)
34. Chuang, J. Y., Kao, T. J., Lin, S. H., Wu, A. C., Lee, P. T., Su, T. P., Yeh, S. H., Lee, Y. C., Wu, C. C., and Chang, W. C. (2017) Specificity protein 1-zinc finger protein 179 pathway is involved in the attenuation of oxidative stress following brain injury. *Redox Biol.* **11**, 135–143 [CrossRef Medline](#)
35. Su, T. C., Lin, S. H., Lee, P. T., Yeh, S. H., Hsieh, T. H., Chou, S. Y., Su, T. P., Hung, J. J., Chang, W. C., Lee, Y. C., and Chuang, J. Y. (2016) The  $\sigma$ -1 receptor-zinc finger protein 179 pathway protects against hydrogen peroxide-induced cell injury. *Neuropharmacology* **105**, 1–9 [CrossRef Medline](#)
36. Wu, C. C., Lee, P. T., Kao, T. J., Chou, S. Y., Su, R. Y., Lee, Y. C., Yeh, S. H., Liou, J. P., Hsu, T. I., Su, T. P., Chuang, C. K., Chang, W. C., and Chuang, J. Y. (2018) Upregulation of Zn179 acetylation by SAHA protects cells against oxidative stress. *Redox Biol.* **19**, 74–80 [CrossRef Medline](#)
37. Lee, Y. C., Huang, W. C., Lin, J. H., Kao, T. J., Lin, H. C., Lee, K. H., Lin, H. C., Shen, C. J., Chang, W. C., and Huang, C. C. (2018) Zn179 E3 ligase-mediated TDP-43 polyubiquitination is involved in TDP-43-ubiquitinated inclusions (UBI) (+)-related neurodegenerative pathology. *J. Biomed. Sci.* **25**, 76 [CrossRef Medline](#)
38. Chang, C. R., and Blackstone, C. (2007) Cyclic AMP-dependent protein kinase phosphorylation of Drp1 regulates its GTPase activity and mitochondrial morphology. *J. Biol. Chem.* **282**, 21583–21587 [CrossRef Medline](#)
39. Cereghetti, G. M., Stangherlin, A., Martins de Brito, O., Chang, C. R., Blackstone, C., Bernardi, P., and Scorrano, L. (2008) Dephosphorylation by calcineurin regulates translocation of Drp1 to mitochondria. *Proc. Natl. Acad. Sci. U.S.A.* **105**, 15803–15808 [CrossRef Medline](#)
40. Cribbs, J. T., and Strack, S. (2007) Reversible phosphorylation of Drp1 by cyclic AMP-dependent protein kinase and calcineurin regulates mitochondrial fission and cell death. *EMBO Rep.* **8**, 939–944 [CrossRef Medline](#)
41. Koch, A., Thiemann, M., Grabenbauer, M., Yoon, Y., McNiven, M. A., and Schrader, M. (2003) Dynamin-like protein 1 is involved in peroxisomal fission. *J. Biol. Chem.* **278**, 8597–8605 [CrossRef Medline](#)
42. Olichon, A., Emorine, L. J., Descoins, E., Pelloquin, L., Bricchese, L., Gas, N., Guillou, E., Delettre, C., Valette, A., Hamel, C. P., Ducommun, B., Lenaers, G., and Belenguer, P. (2002) The human dynamin-related protein OPA1 is anchored to the mitochondrial inner membrane facing the inter-membrane space. *FEBS Lett.* **523**, 171–176 [CrossRef Medline](#)
43. Frezza, C., Cipolat, S., Martins de Brito, O., Micaroni, M., Beznoussenko, G. V., Rudka, T., Bartoli, D., Polishuck, R. S., Danial, N. N., De Strooper, B., and Scorrano, L. (2006) OPA1 controls apoptotic cristae remodeling independently from mitochondrial fusion. *Cell* **126**, 177–189 [CrossRef Medline](#)
44. Amutha, B., Gordon, D. M., Gu, Y., and Pain, D. (2004) A novel role of Mgm1p, a dynamin-related GTPase, in ATP synthase assembly and cristae formation/maintenance. *Biochem. J.* **381**, 19–23 [CrossRef Medline](#)
45. Chang, C. R., and Blackstone, C. (2010) Dynamic regulation of mitochondrial fission through modification of the dynamin-related protein Drp1. *Ann. N.Y. Acad. Sci.* **1201**, 34–39 [CrossRef Medline](#)
46. Del Dotto, V., Fogazza, M., Carelli, V., Rugolo, M., and Zanna, C. (2018) Eight human OPA1 isoforms, long and short: what are they for? *Biochim. Biophys. Acta Bioenerg.* **1859**, 263–269 [CrossRef Medline](#)
47. Zurita Rendón, O., and Shoubbridge, E. A. (2018) LONP1 is required for maturation of a subset of mitochondrial proteins, and its loss elicits an integrated stress response. *Mol. Cell. Biol.* **38**, e00412-17 [CrossRef Medline](#)
48. Yoon, Y., Pitts, K. R., Dahan, S., and McNiven, M. A. (1998) A novel dynamin-like protein associates with cytoplasmic vesicles and tubules of the endoplasmic reticulum in mammalian cells. *J. Cell Biol.* **140**, 779–793 [CrossRef Medline](#)
49. Karbowski, M., Arnoult, D., Chen, H., Chan, D. C., Smith, C. L., and Youle, R. J. (2004) Quantitation of mitochondrial dynamics by photolabeling of individual organelles shows that mitochondrial fusion is blocked during the Bax activation phase of apoptosis. *J. Cell Biol.* **164**, 493–499 [CrossRef Medline](#)
50. Roche, K. W., and Huganir, R. L. (1995) Synaptic expression of the high-affinity kainate receptor subunit KA2 in hippocampal cultures. *Neuroscience* **69**, 383–393 [CrossRef Medline](#)
51. Holtzclaw, L. A., Pandhit, S., Bare, D. J., Mignery, G. A., and Russell, J. T. (2002) Astrocytes in adult rat brain express type 2 inositol 1,4,5-trisphosphate receptors. *Glia* **39**, 69–84 [CrossRef Medline](#)
52. Aceti, M., Creson, T. K., Vaissiere, T., Rojas, C., Huang, W. C., Wang, Y. X., Petralia, R. S., Page, D. T., Miller, C. A., and Rumbaugh, G. (2015) Syngap1 haploinsufficiency damages a postnatal critical period of pyramidal cell structural maturation linked to cortical circuit assembly. *Biol. Psychiatry* **77**, 805–815 [CrossRef Medline](#)
53. Snyder, J. S., Glover, L. R., Sanzone, K. M., Kamhi, J. F., and Cameron, H. A. (2009) The effects of exercise and stress on the survival and maturation of adult-generated granule cells. *Hippocampus* **19**, 898–906 [CrossRef Medline](#)
54. Schmittgen, T. D., and Livak, K. J. (2008) Analyzing real-time PCR data by the comparative  $C(T)$  method. *Nat. Protoc.* **3**, 1101–1108 [CrossRef Medline](#)
55. Fukasawa, Y., Tsuji, J., Fu, S. C., Tomii, K., Horton, P., and Imai, K. (2015) MitoFates: improved prediction of mitochondrial targeting sequences and their cleavage sites. *Mol. Cell. Proteomics* **14**, 1113–1126 [CrossRef Medline](#)
56. Claros, M. G., and Vincens, P. (1996) Computational method to predict mitochondrially imported proteins and their targeting sequences. *Eur. J. Biochem.* **241**, 779–786 [CrossRef Medline](#)
57. Emanuelsson, O., Nielsen, H., Brunak, S., and von Heijne, G. (2000) Predicting subcellular localization of proteins based on their N-terminal amino acid sequence. *J. Mol. Biol.* **300**, 1005–1016 [CrossRef Medline](#)